

Stacking-Dependent Interlayer Coupling in Trilayer MoS₂ with Broken Inversion Symmetry

Jiaxu Yan,[†] Juan Xia,[†] Xingli Wang,[‡] Lei Liu,[§] Jer-Lai Kuo,^{||} Beng Kang Tay,[‡] Shoushun Chen,[⊥] Wu Zhou,[#] Zheng Liu,^{‡,∇} and Ze Xiang Shen^{*,†,●}

[†]Division of Physics and Applied Physics, School of Physical and Mathematical Sciences, Nanyang Technological University, Singapore 637371, Singapore

[‡]NOVITAS, Nanoelectronics Centre of Excellence, School of Electrical and Electronic Engineering, Nanyang Technological University, Singapore 639798, Singapore

[§]State Key Laboratory of Luminescence and Applications, Changchun Institute of Optics, Fine Mechanics and Physics, Chinese Academy of Sciences, Changchun 130033, P. R. China

^{||}Institute of Atomic and Molecular Sciences, Academia Sinica, Taipei 10617, Taiwan

[⊥]School of Electrical and Electronic Engineering, Nanyang Technological University, Singapore 639798, Singapore

[#]Materials Science and Technology Division, Oak Ridge National Laboratory, Oak Ridge, Tennessee 37831, United States

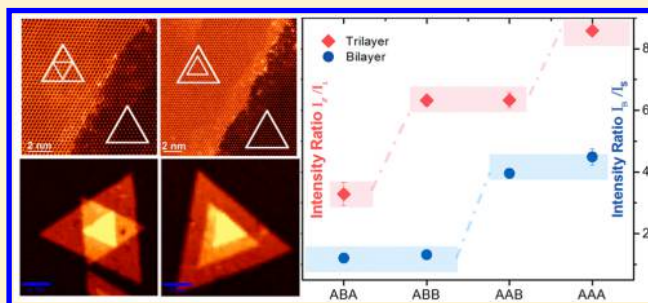
[∇]School of Materials Science and Engineering, Nanyang Technological University, Singapore 639798, Singapore

[●]Centre for Disruptive Photonic Technologies, Nanyang Technological University, Singapore 637371, Singapore

Supporting Information

ABSTRACT: The stacking configuration in few-layer two-dimensional (2D) materials results in different structural symmetries and layer-to-layer interactions, and hence it provides a very useful parameter for tuning their electronic properties. For example, ABA-stacking trilayer graphene remains semimetallic similar to that of monolayer, while ABC-stacking is predicted to be a tunable band gap semiconductor under an external electric field. Such stacking dependence resulting from many-body interactions has recently been the focus of intense research activities. Here we demonstrate that few-layer MoS₂ samples grown by chemical vapor deposition with different stacking configurations (AA, AB for bilayer; AAB, ABB, ABA, AAA for trilayer) exhibit distinct coupling phenomena in both photoluminescence and Raman spectra. By means of ultralow-frequency (ULF) Raman spectroscopy, we demonstrate that the evolution of interlayer interaction with various stacking configurations correlates strongly with layer-breathing mode (LBM) vibrations. Our ab initio calculations reveal that the layer-dependent properties arise from both the spin-orbit coupling (SOC) and interlayer coupling in different structural symmetries. Such detailed understanding provides useful guidance for future spintronics fabrication using various stacked few-layer MoS₂ blocks.

KEYWORDS: Molybdenum disulfide, stacking, ultralow-frequency Raman spectroscopy, photoluminescence, first-principles calculations



In 2D materials, stacking affects the nature of electronic properties by means of the number of layers and their stacking configurations.^{1–5} In principle, stacking governs the crystal symmetry and hence the Coulomb interactions which are crucial in mediating magnetism, superconductivity, and other physical properties.⁶ Such stacking-dependent effects are obviously projected onto transition-metal dichalcogenides (TMDs).^{7–12} As an archetypal TMD, MoS₂ undergoes a transition from the direct-band gap (monolayer) to indirect-band gap semiconductor (few-layer and bulk).^{7,8,13} This crossover of bandgap in MoS₂ gives rise to its exotic electronic and optical properties and make it a promising material for the next-generation electronics and optoelectronics. Apart from the changes of electronic properties, another intriguing character

related to valley polarization is also mediated by stacking configurations.^{9,11,12,14} In even-layer TMD samples, the introduction of inversion symmetry and time-reversal symmetry ensures that the electronic states are doubly spin-degenerate. However, the inversion symmetry is broken in these TMDs with odd-layers, resulting in the splitting of valence bands due to spin-orbit couplings (SOC). Specific to monolayer MoS₂, the SOC splits the valence bands by 160 meV with opposite spin signs in the vicinity of K (K') valley. Together with the time-reversal symmetry, the spin and valley are inherently

Received: September 7, 2015

Revised: November 13, 2015

Published: November 13, 2015

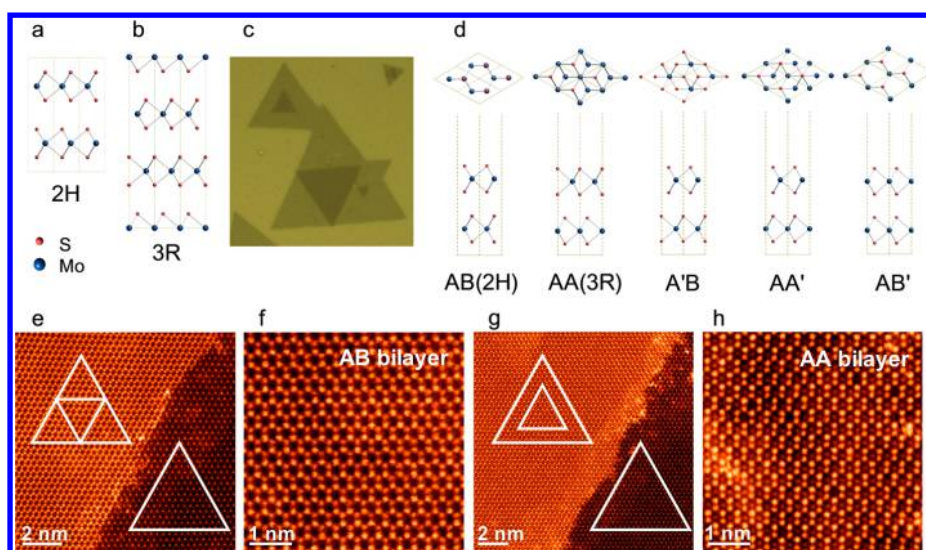


Figure 1. Atomic structures and STEM Z-contrast imaging of bilayer MoS₂. (a,b) Stick-and-ball lattice structure (side view) of layered MoS₂ with typical 2H phase (a) and 3R phase (b). S atoms are shown as red spheres, while Mo atoms sandwiched by two S atomic layers in each unit cell are presented by blue spheres. (c) The optical reflection image of measured AA- and AB bilayer MoS₂. (d) All five classical atomic structures of bilayer MoS₂. (e,f) Z-contrast images of the step edge of AB-stacking MoS₂ bilayer (f) and monolayer. (g,h) Z-contrast images of the step edge of AA-stacking MoS₂ bilayer (h) and monolayer, where the three sites in the AA stacking are Mo (top layer) + S₂ (bottom layer), Mo (bottom layer), and S₂ (top layer) with decreasing image intensity. The two triangles indicate the orientation of the top and bottom MoS₂ layer.

coupled, leading to valley-contrasting optical dichroism. Consequently, one can selectively excite or detect the carriers using left (right) circularly polarized light at K (K') valley, making monolayer MoS₂ the ideal material for valleytronic.¹²

Unlike monolayer MoS₂, 2H bilayer MoS₂ is inversion symmetric, and the valley-contrasting optical selection rule becomes invalid.¹¹ Recently, pioneering experiments have demonstrated that valley-dependent spin polarization can be realized in noncentrosymmetric phases including 3R phase or folded bilayer,^{15,16} bilayer systems by breaking inversion symmetry using a perpendicular electric field.¹⁷ Such manipulation of intrinsic symmetry and spin in even-layer or bulk TMDs has greatly enriched the scope of valley physics and plays a crucial role toward spintronics and valleytronics.

Figure 1a and b shows the two natural polytypes of MoS₂, 2H (space group: *P6₃/mmc*) and 3R (space group: *R3m*), respectively, both of which have trigonal prismatic coordination of the Mo atoms but with distinct stacking orders. In the 2H polytype, the S (Mo) atoms of each layer reside upon the Mo (S) atoms of the other layer, and the bottom layer is fully eclipsed. The 3R polytype consists of three staggered layers, where the S atoms of the middle layer are situated above the Mo atoms of the bottom layer and below the hollow sites of the top layer. In practice, few-layer MoS₂ grown via the bottom-up approach, e.g., by chemical vapor deposition (CVD), may exhibit various stacking orders with interlayer rotations (see Figure 1c for bilayers and Figure 3a for trilayers). The optical images show that CVD grown bilayer MoS₂ sheets typically exhibit two configurations: two triangles in the same orientation (marked as AA) and in reverse orientation (marked as AB). In the trilayer samples, there are four typical stacking patterns: ABA, AAA, AAB, and ABB. Note that the nomenclature we used here is based on the macroscopic geometries based on the optical images directly, which are not necessarily reflection of the atomic stacking configurations.^{18,19} On the other hand, it is imperative to establish direct correlation between the optical images and the atomic

structures. Recently, a related work using optical second-harmonic generation (SHG) measurements found that the AB-stacked bilayer was 2H phase, while the AA-stacked bilayer was 3R phase.^{19,20} In this Letter, we first identify the stacking configurations of various CVD grown MoS₂ trilayer samples using ULF Raman spectroscopy approach and aberration-corrected scanning transmission electron microscopy (STEM). We adopt the Raman spectra and intensity mappings in terms of *A_{1g}* and *E_{2g}¹* vibration modes to characterize the thickness of the MoS₂ flakes used in our experiments. Combining with the first-principles calculations, we reveal the stacking-dependent coupling behaviors in photoluminescence and Raman spectra. We also find that spin-polarized electronic states can be mediated by adopting different stacking orders. Our study broadens the scope of 2D TMD research and uncovers the critical role of stacking on the electronic properties in few-layer MoS₂.

As shown in Figure 1d, we consider all five high-symmetry stacking configurations for bilayer MoS₂, which can be classified into two groups depending on whether the S (Mo) atoms in the top layer are directly situated above the Mo (S) atoms of the bottom layer. As a direct and powerful tool to examine the crystal atomic structures, STEM can provide real space images at the atomic scale with single atom resolution. Such technology has been successfully employed to characterize a large variety of 2D materials including graphene,^{21–23} BN,^{24–26} and TMDs,^{27–29} especially for defect analysis. Our STEM images clearly show the distinct arrangements between AA and AB stacking bilayers (Figure 1e–h). It is because the intensity sensitively relies on the atomic weight and the number of layer. In general, the high intensity sites correspond to the heavy atoms (Mo) and thicker samples, leading a contrast step edge. As shown in Figure 1e and g, there is an obvious contrast boundary across the monolayer and bilayer regions. Figure 1f and h show the Z-contrast images of AB and AA stacking bilayers. The alternant bright and dark columns within the hexagonal lattice represent the 2H stacking, in which the bright

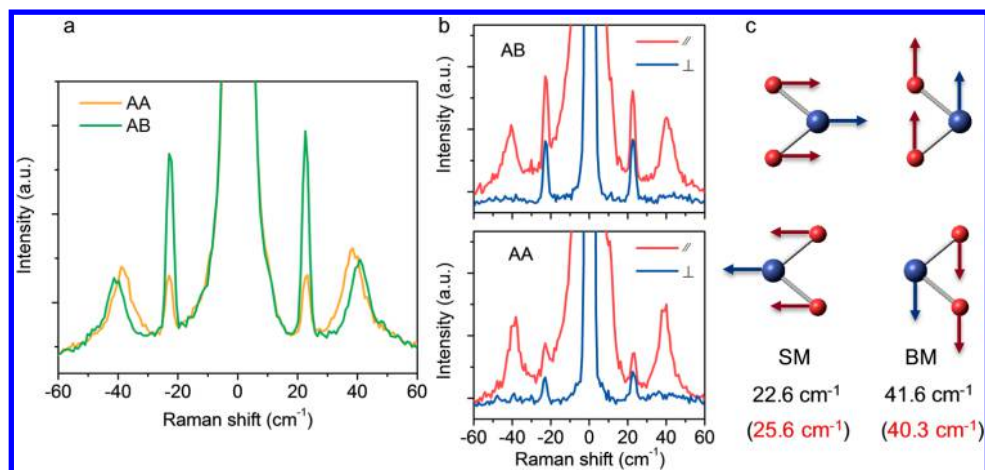


Figure 2. Shear and interlayer breathing vibration behaviors of AA and AB bilayer MoS₂. (a–c) Stokes and anti-Stokes low wavenumber Raman spectra of AA and AB bilayer MoS₂ taken without polarization (a), and under the $\bar{z}(xx)z$ and $\bar{z}(xy)z$ polarized backscattering configurations of AB-stacking bilayer MoS₂ (b) and AA-stacking bilayer MoS₂ (c), respectively. The red and blue curves show the in-plane collection (\parallel) and out-of-plane collection (\perp), respectively. The peak structures are assigned as shear modes (left peak) and interlayer breathing modes (right peak) of bilayer MoS₂, respectively. (d) Vibrational schematics of shear modes (left panel) and interlayer breathing modes (right panel) in bilayer MoS₂ corresponding to the two anti-Stokes peaks in b and c, respectively. The numerical values inserted below are taken from experiments (black) and calculations (red) separately which shows great matching. All of the Raman experiments were conducted using a 532 nm laser.

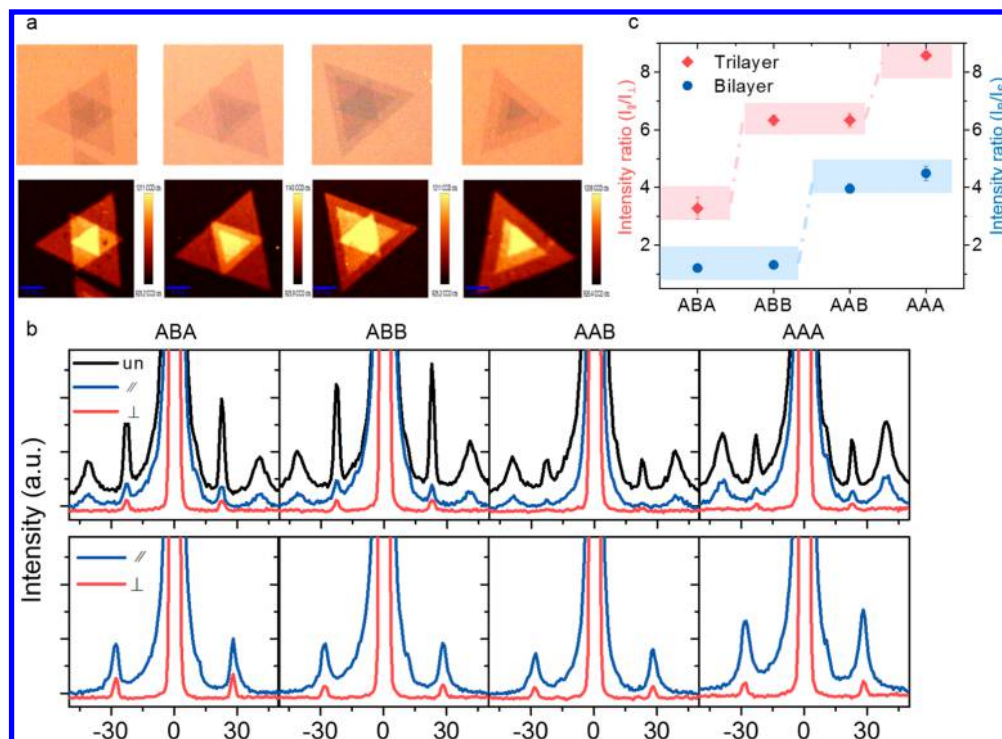


Figure 3. Structural characterization of ABA, ABB, AAB, and AAA trilayer MoS₂. (a, Upper panel) Optical micrograph of trilayer MoS₂ with four different stackings ABA, ABB, AAB, and AAA. (a, Lower panel) Raman intensity mappings of corresponding samples in (a) and the color bar inserted beside. (b, Upper panel) The low wavenumber Raman spectra of the second layer of trilayer MoS₂. The measurement region corresponds to the second layer in (a). (b, Lower panel) The low wavenumber Raman spectra of the third layer of trilayer MoS₂ in (a). (c) The intensity ratio of the interlayer breathing mode and shear mode (blue dots) for bilayer MoS₂, and the $\bar{z}(xx)z$ (\parallel) and $\bar{z}(xy)z$ (\perp) collection (red dots) for trilayer MoS₂ with error bars of experimental standard deviation for several samples.

columns are the Mo (S) atoms of the top layer with the overlaid S (Mo) atoms of the bottom layer. In the AA stacking (3R-like) regions, the brightest are the Mo atoms of the top layer with the overlaid S atoms of the bottom layer, the less bright are the Mo atoms of the bottom layer, and the least bright in the hollow sites are the S atoms of the top layer. The possibility of the metastable A'B stacking here can be ruled out:

although the hollow sites are filled from the top view similar to AA stacking, the images should possess the alternative bright and dark columns (two Mo and two S atoms from each layer), rather than three decreasing image intensity in Figure 1h. Therefore, the STEM images unambiguously provides an identification of the stacking orders in bilayer MoS₂. We calculated the total energies and phonon dispersions of all five

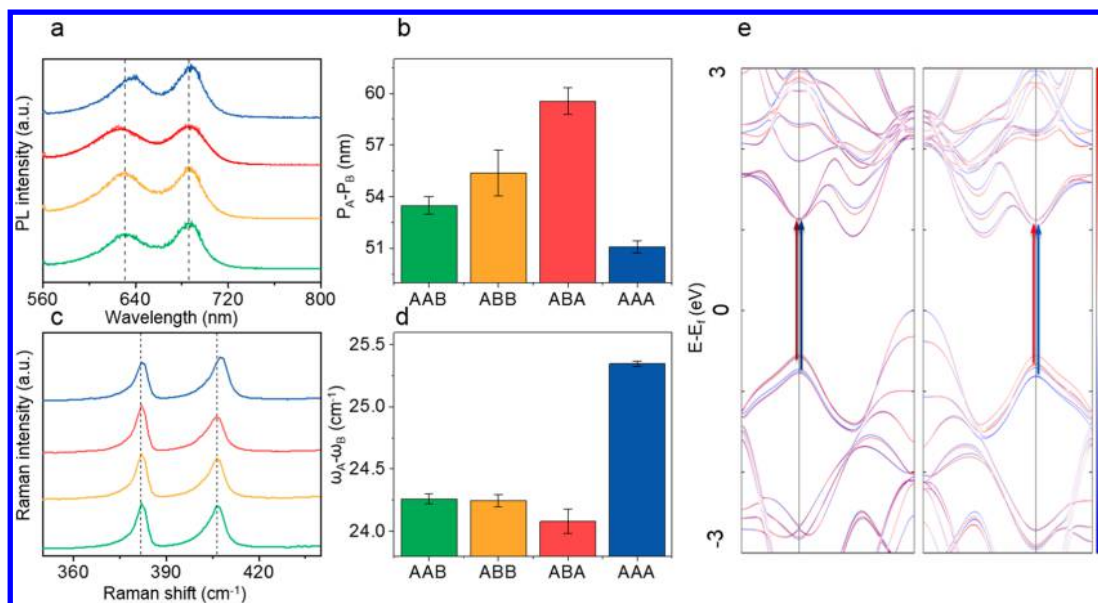


Figure 4. Effects of stacking configuration on the band structure of trilayer MoS₂. (a) Photoluminescence spectra of ABA-, ABB-, AAB-, and AAA-stacking trilayer MoS₂. (b) Stacking dependence of the PL peak separation between P_A and P_B of trilayer MoS₂ with error bars of experimental standard deviation for several samples. (c) Raman spectra of ABA-, ABB-, AAB-, and AAA-stacking trilayer MoS₂. (d) Stacking dependence of the Raman peak separation between A_{1g} and E_{2g}¹ of trilayer MoS₂ with error bars of experimental standard deviation for several samples. All spectra are acquired using 532 nm laser. (e) Schematics of calculated band structure of ABA- (left panel) and AAA-stacking (right panel) trilayer MoS₂. The band curves in red and blue correspond to the spin-up and spin-down states, respectively.

configurations, as shown in [Supplementary Figure S2](#). Our results indicate that AB' and AA' are energetically unfavorable among all configurations because the S atoms of one layer are placed directly above the S atoms of the other layer. Due to the strong repulsion between the S atoms, these two stacking configurations are dynamically unstable with imaginary frequencies in the gamma point. The other three configurations have lower energy and are dynamically stable with distinct frequencies of Raman modes, especially in the ULF region ([Supplementary Figure S2](#)). The A'B configuration has two ULF peaks at ~ 16.6 and ~ 32.0 cm⁻¹ belonging to the in-plane shear mode and out-of-plane breathing mode, respectively. These two modes are found at ~ 25.6 (~ 26.0) and ~ 40.3 cm⁻¹ (~ 38.3) in the AB (AA) configuration. Compared to our experimental Raman spectra shown in [Figure 2a](#), the frequency values and the relative peak position changes are at ~ 22.6 (~ 22.8) and ~ 41.6 (~ 38.7) cm⁻¹, in excellent agreement with the calculated results of two most stable configurations (AB and AA stacking). Thus, another dynamically stable metastable A'B configuration is excluded. We also note that the shear mode only red shift a little, while the breathing mode blue shift from AB to AA stacking. As for the peak position shift, we analyzed the force constants in AB- and AA- stacking bilayer MoS₂ up to the second-nearest neighbors. As shown in [Figure S5](#), the stacking sequence not only changes the interactions between the two layers (k_{34}), but also involves the interactions up to the second-nearest neighbors (k_{24}). The calculated force constants are listed in [Table S1](#). First, the force constants which determine the in-plane shear modes (SM) are smaller than those of the out-of-plane breathing modes (BM). That is the reason for the stronger shift in BM rather than SM. Furthermore, the stacking affects both k_{24} and k_{34} , leading to the different behaviors for BM and SM. For instance, for BM, the force constant of k_{34} increases, but k_{24} decreases significantly between AB and AA stackings, resulting in the

red shift of BM. However, the SM are not sensitive to stacking, which can be attributed to the almost equal change in force constant of k_{34} (decreasing) and k_{24} (increasing) between AB and AA stacking. More importantly, the intensity ratio between the breathing mode and shear mode is very distinct: ~ 1.2 for AB and ~ 4.1 for AA stacking, calculated using the integrated areas of the Stokes Raman peaks. We also performed the polarized Raman measurements in backscattering configurations with parallel and crossed polarization geometry. As shown in [Figure 2b](#), in the crossed geometry, all breathing modes are forbidden.³⁰ The relative intensity ratio of shear modes to breathing modes is consistent with unpolarized measurements. The Raman spectra for AA and AB configurations within the high-frequency range (around 400 cm⁻¹) as well as the photoluminescence (PL) spectra are also shown in [Supplementary Figure S6](#). There is no prominent stacking-dependence in the high-frequency range. Therefore, the ratio of shear modes to breathing modes in the ULF range (< 50 cm⁻¹) can conveniently identify the stacking orders of bilayer MoS₂, and also confirm our previous STEM results and first-principles calculations: macroscopic AA and AB stacking patterns correspond to 3R-like and 2H atomic stacking orders, respectively.

We now turn to study the trilayer systems. [Figure 3a](#) shows the optical images of CVD grown trilayer MoS₂ with four different stackings, ABA, ABB, AAB, and AAA following the nomenclature of bilayer system. The layer number is precisely determined using Raman intensity mappings of corresponding samples. The corresponding Raman profiles with intensity changes are plotted in [Supporting Information](#). Before identification of the stacking configurations for trilayer systems, we first examine the bottom two layers in the trilayer MoS₂ samples. As mentioned above, we can identify the stacking orders of bilayer region using the relative intensity of breathing modes and shear modes by integrating the peak areas. Indeed,

as shown in Figure 3b, the ratio of the intensity of BM to that of SM (I_b/I_s) can be used to classify the bilayer regions of the four trilayer samples (ABA, ABB, AAB, AAA stacking) into two groups: the first two stackings (ABA and ABB) with $I_b/I_s = \sim 1$ could be classified as AB stacking for the bilayer, while the last two stackings (AAB and AAA) with $I_b/I_s = \sim 4$ should be considered as AA stacking, respectively, which are in perfect agreement with previous bilayer results. Based on the above bilayer results, we now construct the atomic structure models for trilayer system (see Supporting Information), in which the ABB and AAB atomic configurations are completely equivalent. The calculated Raman-active modes in both low and high frequencies of all configurations are given and match well with the experimental data. As shown in Figure 3b, we find the shear modes and the breathing modes in ULF range are almost merged into one peak, where I_b/I_s cannot be directly used to identify the stacking configurations. In order to quantify the difference between the two modes, we use the polarization measurements to identify the different features between the shear mode and breathing $I_{//}/I_{\perp}$ mode. Here, $I_{//}$ is the summation of the parallel components of both shear mode and breathing mode, while I_{\perp} contains only the perpendicular component of shear mode, as the breathing mode is entirely suppressed under perpendicular collection configuration. Thus, I_b/I_s in bilayer systems changes to $I_{//}/I_{\perp}$ for the trilayer systems. By changing the stacking orders we find the intensity ratio $I_{//}/I_{\perp}$ for AAA stacking is most dramatically reduced, followed by AAB (ABB) stacking, with ABA stacking changes the least. We summarize the intensity ratios of the interlayer breathing modes to shear modes for bilayer (~ 1 for AB stacking and ~ 4 for AA stacking) and trilayer MoS₂ (~ 3 for ABA stacking, ~ 6 for AAB and ABB stacking, ~ 8 for AAA stacking) in Figure 3c. Obviously, the intensity ratio is stacking-dependent for both bilayer and trilayer MoS₂, which can be used to identify the stacking orders in few-layer MoS₂.

Now we turn to examine the interlayer coupling in different stackings for the trilayer samples. Figure 4a plots the photoluminescence (PL) spectra of a set of trilayer MoS₂ with various stackings. Figure 4b shows the stacking dependence of the PL peak separation between two prominent peaks P_A and P_B , which attribute to the A and B excitons generated by the direct transitions from the edges of two splitting valence bands to the conduction bands at K points. Interestingly, the splitting in ABA stacking samples is the largest (~ 62 nm), followed by those with ABB (AAB) stacking (~ 56 nm), while AAA stacking has the smallest splitting (48 nm). A similar trend is also found in our bilayer systems with AA and AB stacking (see SI). Such stacking-dependent splitting patterns in few-layer samples arise as a resultant of the spin-orbit coupling and the interlayer hopping effects. In even-layer samples with inversion symmetry, both SOC and interlayer hopping effects contribute to the splitting between A and B peaks at K points. The different behaviors in splitting patterns have been reported in optical reflection spectra and transmission spectra for the 2H and 3R bulk phases.^{15,31}

As for the Raman vibration modes in the high frequency region, distinct behaviors also exhibit in Figure 4c,d. The in-plane E_{2g}^1 modes almost remain unchanged, while the out-of-plane A_{1g} modes blue shift with altering the 2H stacking, leading to the largest frequency difference in AAA stacking samples (~ 25.35 cm⁻¹), followed by AAB (ABB) trilayer (~ 24.25 cm⁻¹), and the smallest in that with ABA stacking (~ 24.07 cm⁻¹). Such stacking-dependent frequency separations

of E_{2g}^1 mode and A_{1g} mode can be understood easily.^{30,32–35} The red shift of E_{2g}^1 modes may be attributed to the long-range Coulombic interlayer interactions, while the blue shift of A_{1g} modes is due to increasing restoring forces as the van der Waals bonds are contracted. For few-layer samples with various stacking orders, each monolayer MoS₂ is identical and just assembled in various sequences, leading to different lateral registrations but almost identical interlayer distances. The stacking-dependent Raman feature manifests the stacking-dependent interlayer coupling, similar to the trend on the layer number.^{30,32–35}

Figure 4e shows the spin-polarized band structures of ABA- and AAA-stacking trilayer MoS₂ considering SOC effects. The band curves in red (blue) represent the spin-up (spin-down) states. SOC effects dominate the energy splitting in the top valence bands for ABA-stacking, while both SOC and interlayer hopping effects contribute to the splitting patterns for AAA-stacking trilayer, which corresponds to the observed stacking-dependent PL peak separation in Figure 4a,b. Another interesting feature is the different spin-valley polarizations in different stackings: the valence band edges at K point in ABA stacking are dominantly from spin-up states with some mixing of spin-down states, while in AAA stacking the VBM bands are completely spin-polarized. Our ab initio calculations indicate the enhanced spin-valley polarization in the AAA stacking contrast to the ABA stacking, which is similar to the observed spin-polarized states in the 3R phase by circularly polarized photoluminescence measurements.¹⁵ In ref 16, the authors have argued that the characters of the valence bands are exchanged between two valleys for 2H stacking, but preserved for 3R stacking. Our first-principles calculations also reproduce such scene for bilayer samples: the charge states are localized within each layer for AA-stacking bilayer, while for AB-stacking the charges are distributed dispersedly among layers (see Figure S12). This suggests that the interlayer hopping in AAA stacking is greatly suppressed, and the circular polarization is not affected. Note that the above calculations do not include SOC effects. Due to the comparable SOC and interlayer hopping, the above simple view becomes vague and the charge density distributions become nonlocal. For tungsten dichalcogenides with giant SOC (~ 0.4 eV), the VBM bands are completely spin-polarized in AAA stacking that are the same as in monolayer and the Bloch states are localized in each layer, because the interlayer hopping is greatly suppressed.

In summary, for the first time we establish the one-to-one correspondence between the macroscopic stacking patterns and the atomic stacking orders, by means of ULF Raman spectroscopy approach and STEM. Our experimental and theoretical results reveal that distinct interlayer coupling behaviors emerge in different structural symmetries, as well as the spin-polarized states. Such findings afford new insight in few-layer 2D systems and provide new possibilities for future spintronics based on various stacking of MoS₂ blocks.

Methods. Sample Preparation. Few-layered MoS₂ nanoflakes were synthesized using chemical vapor deposition (CVD) technology. For the growth, 1g MoS₂ in a ceramic boat was put at the center of a 1 in. quartz tube with a piece of SiO₂/Si wafer (1×10 cm²) following behind. The system was pumped down to 30 Torr before heated up to 900 °C in 35 min; the pressure remained at 30 Torr for another 10 min, then increased to 760 Torr in 1 min, and remained for another 20 min. After the reaction, the system was cooled down to room temperature naturally. 20 sccm Ar was used as the carrier gas.

Raman Spectra and Photoluminescence Measurements.

For all of the optical contrast images and Raman single spectra, Raman intensity mappings, as well as PL spectra at room temperature as shown in Figures 1–4 and Figures S6, S8–S11, we use a Witec CRM200 backscattering Raman system equipped with a solid-state YAG laser at 2.33 eV with a proper power avoiding sample heating (below 1 mW). The size of the laser beam is around 250 nm which was focused on the sample using an objective (Olympus, 100 \times /NA0.95). For ultralow-frequency Raman spectra, we use two BraggGrate Notch Filters (BNF) centered at 532 nm with bandwidths as narrow as 5 cm⁻¹ and a large OD (>4) to achieve low frequency region. Meanwhile, a linear polarizer with different collection angles was used to realize the parallel ($\bar{z}(xx)z$) and perpendicular ($\bar{z}(xy)z$) and backscattering configurations, respectively.

Ab Initio Calculations. The first-principles calculations to compute the electronic structures are performed with the plane wave basis set as implemented in the QUANTUM ESPRESSO program package.³⁶ The norm-conserving pseudopotentials,³⁷ including spin–orbit coupling effects, were adopted, and a cutoff energy for the basis set was 140 Ry. The exchange correlation potential was described using the local-density approximation in the parametrization of Perdew and Zunger.³⁸ The Brillouin zone was sampled by a 15 \times 15 \times 1 *k*-point mesh. The energy convergence for the relaxation was chosen to be less than 10⁻⁵ eV/Å. A 20 Å vacuum layer along the *z*-axis is added to avoid the mirror interactions between the neighboring images. We calculated the phonon spectrum and Raman intensities within density-functional perturbation theory (DFPT).³⁹ To do the spin projection calculations, we computed the Wannier functions by the maximally localized algorithm,⁴⁰ implemented in the package WANNIER90⁴¹ using Mo *d* orbitals and S *p* orbitals. Taking account of nonlocal van der Waals interaction, we adopted the newly developed vdW density functional (vdW-DF) in our study.^{42–44}

■ ASSOCIATED CONTENT

Supporting Information

The Supporting Information is available free of charge on the ACS Publications website at DOI: 10.1021/acs.nanolett.5b03597.

Role of van der Waals interaction in the first-principles calculations, few-layer MoS₂ sample preparation, force constants model for bilayer MoS₂, Raman spectra and photoluminescence spectra of bilayer and trilayer MoS₂, the atomic structures of trilayer MoS₂, the gamma-point phonon frequencies and the charge density distributions in trilayer MoS₂ (PDF)

■ AUTHOR INFORMATION

Corresponding Author

*E-mail: zexiang@ntu.edu.sg.

Author Contributions

J.X. performed the experiments. J.Y. performed simulation studies. X.W. and Z.L. helped to prepare the samples. W.Z. provided the STEM images. All authors discussed the results. L.L. and J.L.K. provided computation resources. J.Y. and Z.X.S. conceived the study. J.Y. and J.X. wrote the manuscript with contributions from coauthors. J.X. and J.Y. contributed equally to this work.

Notes

The authors declare no competing financial interest.

■ ACKNOWLEDGMENTS

This research was supported by MOE under AcRF Tier 2 (MOE2012-T2-2-124) and AcRF Tier 3 (MOE2011-T3-1-005) in Singapore. X.W. and B.K.T. would like to acknowledge the funding support from NTU-A*STAR Silicon Technologies Centre of Excellence under the program grant No. 112 3510 0003. The electron microscopy work was supported by the U.S. Department of Energy, Office of Science, Basic Energy Science, Materials Sciences and Engineering Division (W.Z.). J.Y. and J.X. acknowledge the technical support from H.L.H at WITec.

■ REFERENCES

- (1) Lee, Y.; Tran, D.; Myhro, K.; Velasco, J.; Gillgren, N.; Lau, C. N.; Barlas, Y.; Poumirol, J. M.; Smirnov, D.; Guinea, F. *Nat. Commun.* **2014**, *5*, 5656.
- (2) Craciun, M. F.; Russo, S.; Yamamoto, M.; Oostinga, J. B.; Morpurgo, A. F.; Tarucha, S. *Nat. Nanotechnol.* **2009**, *4* (6), 383–388.
- (3) Bao, W.; Jing, L.; Velasco, J.; Lee, Y.; Liu, G.; Tran, D.; Standley, B.; Aykol, M.; Cronin, S. B.; Smirnov, D.; Koshino, M.; McCann, E.; Bockrath, M.; Lau, C. N. *Nat. Phys.* **2011**, *7* (12), 948–952.
- (4) Lui, C. H.; Li, Z.; Mak, K. F.; Cappelluti, E.; Heinz, T. F. *Nat. Phys.* **2011**, *7* (12), 944–947.
- (5) Zhang, W. J.; Yan, J. X.; Chen, C. H.; Lei, L.; Kuo, J. L.; Shen, Z. X.; Li, L. *J. Nat. Commun.* **2013**, *4*, 8.
- (6) Yacoby, A. *Nat. Phys.* **2011**, *7* (12), 925–926.
- (7) Splendiani, A.; Sun, L.; Zhang, Y.; Li, T.; Kim, J.; Chim, C.-Y.; Galli, G.; Wang, F. *Nano Lett.* **2010**, *10* (4), 1271–1275.
- (8) Mak, K. F.; Lee, C.; Hone, J.; Shan, J.; Heinz, T. F. *Phys. Rev. Lett.* **2010**, *105* (13), 136805.
- (9) Xiao, D.; Liu, G.-B.; Feng, W.; Xu, X.; Yao, W. *Phys. Rev. Lett.* **2012**, *108* (19), 196802.
- (10) Cao, T.; Wang, G.; Han, W.; Ye, H.; Zhu, C.; Shi, J.; Niu, Q.; Tan, P.; Wang, E.; Liu, B.; Feng, J. *Nat. Commun.* **2012**, *3*, 887.
- (11) Mak, K. F.; He, K.; Shan, J.; Heinz, T. F. *Nat. Nanotechnol.* **2012**, *7* (8), 494–498.
- (12) Xu, X.; Yao, W.; Xiao, D.; Heinz, T. F. *Nat. Phys.* **2014**, *10* (5), 343–350.
- (13) Sun, L. F.; Hu, H. L.; Zhan, D.; Yan, J. X.; Liu, L.; Teguh, J. S.; Yeow, E. K. L.; Lee, P. S.; Shen, Z. X. *Small* **2014**, *10* (6), 1090–1095.
- (14) Zeng, H.; Dai, J.; Yao, W.; Xiao, D.; Cui, X. *Nat. Nanotechnol.* **2012**, *7* (8), 490–493.
- (15) Suzuki, R.; Sakano, M.; Zhang, Y. J.; Akashi, R.; Morikawa, D.; Harasawa, A.; Yaji, K.; Kuroda, K.; Miyamoto, K.; Okuda, T.; Ishizaka, K.; Arita, R.; Iwasa, Y. *Nat. Nanotechnol.* **2014**, *9* (8), 611–617.
- (16) Jiang, T.; Liu, H.; Huang, D.; Zhang, S.; Li, Y.; Gong, X.; Shen, Y.-R.; Liu, W.-T.; Wu, S. *Nat. Nanotechnol.* **2014**, *9* (10), 825–829.
- (17) Yuan, H.; Bahramy, M. S.; Morimoto, K.; Wu, S.; Nomura, K.; Yang, B.-J.; Shimotani, H.; Suzuki, R.; Toh, M.; Kloc, C.; Xu, X.; Arita, R.; Nagaosa, N.; Iwasa, Y. *Nat. Phys.* **2013**, *9* (9), 563–569.
- (18) Cao, B.; Li, T. *J. Phys. Chem. C* **2015**, *119* (2), 1247–1252.
- (19) Hsu, W.-T.; Zhao, Z.-A.; Li, L.-J.; Chen, C.-H.; Chiu, M.-H.; Chang, P.-S.; Chou, Y.-C.; Chang, W.-H. *ACS Nano* **2014**, *8* (3), 2951–2958.
- (20) Liu, K.; Zhang, L.; Cao, T.; Jin, C.; Qiu, D.; Zhou, Q.; Zettl, A.; Yang, P.; Louie, S. G.; Wang, F. *Nat. Commun.* **2014**, *5*, 4966.
- (21) Gong, Y.; Shi, G.; Zhang, Z.; Zhou, W.; Jung, J.; Gao, W.; Ma, L.; Yang, Y.; Yang, S.; You, G.; Vajtai, R.; Xu, Q.; MacDonald, A. H.; Yakobson, B. I.; Lou, J.; Liu, Z.; Ajayan, P. M. *Nat. Commun.* **2014**, *5*, 3193.
- (22) Liu, Z.; Ma, L.; Shi, G.; Zhou, W.; Gong, Y.; Lei, S.; Yang, X.; Zhang, J.; Yu, J.; Hackenberg, K. P.; Babakhani, A.; Idrobo, J.-C.; Vajtai, R.; Lou, J.; Ajayan, P. M. *Nat. Nanotechnol.* **2013**, *8* (2), 119–124.
- (23) Hashimoto, A.; Suenaga, K.; Gloter, A.; Urita, K.; Iijima, S. *Nature* **2004**, *430* (7002), 870–873.
- (24) Krivanek, O. L.; Chisholm, M. F.; Nicolosi, V.; Pennycook, T. J.; Corbin, G. J.; Dellby, N.; Murfitt, M. F.; Own, C. S.; Szilagy, Z. S.;

Oxley, M. P.; Pantelides, S. T.; Pennycook, S. J. *Nature* **2010**, *464* (7288), 571–574.

(25) Liu, Z.; Gong, Y.; Zhou, W.; Ma, L.; Yu, J.; Idrobo, J. C.; Jung, J.; MacDonald, A. H.; Vajtai, R.; Lou, J.; Ajayan, P. M. *Nat. Commun.* **2013**, *4*, 2541.

(26) Haigh, S. J.; Gholinia, A.; Jalil, R.; Romani, S.; Britnell, L.; Elias, D. C.; Novoselov, K. S.; Ponomarenko, L. A.; Geim, A. K.; Gorbachev, R. *Nat. Mater.* **2012**, *11* (9), 764–767.

(27) Lin, Y.-C.; Dumcenco, D. O.; Huang, Y.-S.; Suenaga, K. *Nat. Nanotechnol.* **2014**, *9* (5), 391–396.

(28) Najmaei, S.; Liu, Z.; Zhou, W.; Zou, X.; Shi, G.; Lei, S.; Yakobson, B. I.; Idrobo, J.-C.; Ajayan, P. M.; Lou, J. *Nat. Mater.* **2013**, *12* (8), 754–759.

(29) Gong, Y.; Lin, J.; Wang, X.; Shi, G.; Lei, S.; Lin, Z.; Zou, X.; Ye, G.; Vajtai, R.; Yakobson, B. I.; Terrones, H.; Terrones, M.; Tay, B. K.; Lou, J.; Pantelides, S. T.; Liu, Z.; Zhou, W.; Ajayan, P. M. *Nat. Mater.* **2014**, *13* (12), 1135–1142.

(30) Boukhicha, M.; Calandra, M.; Measson, M.-A.; Lancry, O.; Shukla, A. *Phys. Rev. B: Condens. Matter Mater. Phys.* **2013**, *87* (19), 195316.

(31) Beal, A. R.; Knights, J. C.; Liang, W. Y. *J. Phys. C: Solid State Phys.* **1972**, *5* (24), 3540.

(32) Luo, X.; Zhao, Y.; Zhang, J.; Xiong, Q.; Quek, S. Y. *Phys. Rev. B: Condens. Matter Mater. Phys.* **2013**, *88* (7), 075320.

(33) Molina-Sánchez, A.; Wirtz, L. *Phys. Rev. B: Condens. Matter Mater. Phys.* **2011**, *84* (15), 155413.

(34) Zeng, H.; Zhu, B.; Liu, K.; Fan, J.; Cui, X.; Zhang, Q. *M. Phys. Rev. B: Condens. Matter Mater. Phys.* **2012**, *86* (24), 241301.

(35) Zhang, X.; Han, W. P.; Wu, J. B.; Milana, S.; Lu, Y.; Li, Q. Q.; Ferrari, A. C.; Tan, P. H. *Phys. Rev. B: Condens. Matter Mater. Phys.* **2013**, *87* (11), 115413.

(36) Giannozzi, P.; Baroni, S.; Bonini, N.; Calandra, M.; Car, R.; Cavazzoni, C.; Ceresoli, D.; Chiarotti, G. L.; Cococcioni, M.; Dabo, I.; Dal Corso, A.; de Gironcoli, S.; Fabris, S.; Fratesi, G.; Gebauer, R.; Gerstmann, U.; Gougoussis, C.; Kokalj, A.; Lazzeri, M.; Martin-Samos, L.; Marzari, N.; Mauri, F.; Mazzarello, R.; Paolini, S.; Pasquarello, A.; Paulatto, L.; Sbraccia, C.; Scandolo, S.; Sclauzero, G.; Seitsonen, A. P.; Smogunov, A.; Umari, P.; Wentzcovitch, R. M. *J. Phys.: Condens. Matter* **2009**, *21* (39), 395502.

(37) Hamann, D. R. *Phys. Rev. B: Condens. Matter Mater. Phys.* **1989**, *40* (5), 2980–2987.

(38) Perdew, J. P.; Zunger, A. *Phys. Rev. B: Condens. Matter Mater. Phys.* **1981**, *23* (10), 5048–5079.

(39) Lazzeri, M.; Mauri, F. *Phys. Rev. Lett.* **2003**, *90* (3), 036401.

(40) Marzari, N.; Vanderbilt, D. *Phys. Rev. B: Condens. Matter Mater. Phys.* **1997**, *56* (20), 12847–12865.

(41) Mostofi, A. A.; Yates, J. R.; Lee, Y.-S.; Souza, I.; Vanderbilt, D.; Marzari, N. *Comput. Phys. Commun.* **2008**, *178* (9), 685–699.

(42) Dion, M.; Rydberg, H.; Schröder, E.; Langreth, D. C.; Lundqvist, B. I. *Phys. Rev. Lett.* **2004**, *92* (24), 246401.

(43) Thonhauser, T.; Cooper, V. R.; Li, S.; Puzder, A.; Hyldgaard, P.; Langreth, D. C. *Phys. Rev. B: Condens. Matter Mater. Phys.* **2007**, *76* (12), 125112.

(44) Román-Pérez, G.; Soler, J. M. *Phys. Rev. Lett.* **2009**, *103* (9), 096102.